Real-time Wireless Sensing and Positioning through Reconfigurable Intelligent Surfaces

Wankai Tang, Shengguo Meng, Qun Yan Zhou, Yifan Xu, Jun Yan Dai, Jie Yang, Kai-Kit Wong, Shi Jin, Qiang Cheng, and Tie Jun Cui

Abstract

Reconfigurable intelligent surface (RIS) has emerged as a promising technology for wireless communication systems due to its ability to manipulate electromagnetic waves. With advantages such as low hardware complexity and low power consumption, RIS shows significant potential in positioning applications. This paper presents an RIS-based wireless signal sensing method that operates under the constraint of passive reflection while leveraging the space-time coding capabilities of RIS. By applying a space-time coding matrix on the RIS, the beamspace domain and the angle of arrival (AoA) of signals incident on the RIS can be efficiently estimated, requiring only the processing of single-channel received signals at the access point. Building upon this, a positioning prototype system utilizing two 27 GHz millimeter-wave RIS panels is developed and implemented, supporting real-time user positioning. Experimental results demonstrate that the prototype system achieves centimeter-level positioning accuracy, with errors below 10 cm in 97.22% of measurement cases, thereby validating the effectiveness of the proposed sensing and positioning scheme. These findings may pave the way for further exploration of RIS-based integration of sensing and communication technologies.

Index Terms

Reconfigurable intelligent surface, wireless sensing, user positioning, millimeter-wave, intelligent reflecting surface, metasurface.

Wankai Tang, Shengguo Meng, Yifan Xu, Jie Yang, and Shi Jin are with the National Mobile Communications Research Laboratory, Southeast University, Nanjing 210096, China (e-mail: tangwk@seu.edu.cn; seumengsg@seu.edu.cn; 220230973@seu.edu.cn; yangjie@seu.edu.cn; jinshi@seu.edu.cn).

Qun Yan Zhou, Jun Yan Dai, Qiang Cheng, and Tie Jun Cui are with the State Key Laboratory of Millimeter Waves, Southeast University, Nanjing 210096, China (e-mail: qyzhou@seu.edu.cn; junyand@seu.edu.cn; qiangcheng@seu.edu.cn; tjcui@seu.edu.cn).

Kai-Kit Wong is with the Department of Electronic and Electrical Engineering, University College London, London WC1E 6BT, United Kingdom (e-mail: kai-kit.wong@ucl.ac.uk).

I. Introduction

As mobile communication systems evolve and upgrade, the air interface transmission performance and data service capabilities are continuously enhanced. However, the sole function of wireless information transmission inevitably faces development bottlenecks. Future mobile communication systems are progressing towards greater intelligence and software-defined functions, with the potential to further expand wireless network capabilities and application scenarios by integrating environmental sensing, user positioning, and the new paradigm of intelligent wireless environments [1], [2].

Nowadays, location-based services have become one of the fastest-growing application areas in the development of mobile internet. Outdoor positioning services have seen unprecedented growth, thanks to the robust support of systems like the global positioning system (GPS) and the BeiDou navigation satellite system, enabling services such as traffic navigation, food delivery, entertainment searches, and more. On the other hand, as modern society increasingly engages in indoor activities, the demand for indoor positioning has risen sharply, for scenarios such as underground parking lots, large shopping malls, and office buildings. Whether in outdoor or indoor environments, the ability to quickly and accurately obtain the location information of mobile users and provide location-based services is becoming increasingly important. Communication and positioning systems are integrating and mutually promoting each other [3].

At the same time, the emerging reconfigurable intelligent surface (RIS) technology, which can reshape the characteristics of the wireless propagation environment, enhances wireless network communication performance [4]. It is also expected to leverage the spatial dimensions provided by its array structure to improve the sensing capabilities of wireless systems, thereby ensuring positioning accuracy and reducing hardware complexity [5], [6]. Against this background, RIS-assisted positioning systems have recently been studied. In early work [7], RIS panels are employed in millimeter-wave wireless communication systems, using multiple subcarriers for user positioning. Numerical simulations show that the more unit cells an RIS has, the higher the positioning accuracy. The authors in [8] analyze the downlink positioning problem, and propose a two-step optimization scheme to select the combination of unit cells of RIS to activate and design their reflection phase shifts, which can improve the system's positioning performance and coverage range. A two-stage positioning method utilizing dual RIS panels is proposed in [9]. Triangulation for positioning is constructed using the delay difference between the direct path

and the reflection path, along with the angles of each path.

The work [10] designs a beam training scheme for RIS-assisted millimeter-wave communication systems to obtain the optimal beams for the base station (BS), RIS, and user. By using the estimated angle information, an iterative positioning algorithm is designed to achieve centimeter-level positioning accuracy. The authors in [11] propose an RIS-aided multi-user positioning protocol based on received signal strength (RSS), and formulate the optimization problem to minimize the weighted probabilities of false positioning. The probability of incorrect positioning can be reduced by optimizing the decision function and RIS phase shifts. The authors in [12] derive the Cramér-Rao lower bound (CRLB) for assessing the positioning and orientation performance and propose an RIS phase shift design which can minimize the CRLB. The problem of direction of arrival (DOA)-based target positioning in an RIS-assisted radar system is studied in [13]. Simulation results validate the efficiency of the proposed estimator that jointly optimizes the reflection coefficients and target DOA. The authors in [14] propose a two-step positioning approach that RIS panels play the role of passive anchors. Theoretical analysis and simulation indicate that RIS has the potential to realize accurate positioning with only a single BS.

In addition to the aforementioned studies focused on theoretical analysis and numerical simulations, some pioneering research explores the design and implementation of positioning prototype systems using RIS hardware. The authors in [15] use an RIS to improve the accuracy of a received signal strength-based positioning system. The algorithm requires pre-built radio maps and shows considerable improvement of positioning accuracy. [16] proposes a Transformer-based device-free sensing scheme for joint people counting and positioning through processing channel state information (CSI). The RIS is utilized to reflect the signals toward the non-line-of-sight (NLoS) regions. A method based on 1-bit RIS and time modulation is proposed in [17] to estimate both azimuth and elevation angles of incident signals, which are important parameters for positioning. The authors in [18] propose a DNN-DANM method for DOA estimation by combining the deep neural network (DNN) and the decoupling atomic norm minimization (DANM). This method takes into account the imperfect aspects of RIS hardware. RIS-assisted positioning is implemented in [19], which leverages real frequency-domain mmWave indoor channel sounding measurements and shows how RIS-reflected paths could contribute to positioning accuracy. The prototype system in [20] includes an RIS, a single-antenna transmitter, and a four-antenna receiver. The inaccurate transmitter position problem and the unknown RIS phase offset problem are investigated and solved.

Existing studies highlight the potential of RIS in the field of positioning. However, theoretical research often assumes perfect knowledge of CSI or incurs additional time overhead for beam scanning. Meanwhile, prototype implementations typically depend on pre-collected data to build radio maps and train neural networks, relying on non-real-time channel measurements, or require leveraging the spatial dimension of a multichannel receiver. These factors impact the feasibility and generalization of the proposed scheme in practical scenarios. The realization of RIS-based real-time wireless signal sensing and positioning remains an area of exploration. This paper presents an RIS-based real-time wireless signal sensing method that efficiently estimates the angle of arrival (AoA) of signals incident on the RIS. Furthermore, a positioning prototype system leveraging two millimeter-wave RIS panels has been designed and implemented. The main contributions of this paper are summarized as follows:

1) We introduce an RIS-based wireless signal sensing method under the constraint of passive reflection characteristics of RIS. The single-channel signal received by the access point is processed to efficiently estimate the wireless channel between the user and the RIS. Notably, we prove that this method is robust against the non-ideal reflection coefficients of RIS's unit cells.
2) We design an RIS-based positioning prototype system. By performing space-time coding matrix, the beamspace domain of signals incident on RIS can be obtained. The system calculates the AoAs from the user to the two RIS panels and thus acquires the user position. The wireless frame structure and the hardware architecture are presented in detail.
3) We implement the prototype system by using two 27 GHz millimeter-wave RIS panels and several hardware modules. The measurement results demonstrate that the proposed scheme achieves centimeter-level accuracy for indoor user positioning. In particular, a positioning error of less than 10 cm is achieved in 97.22% of the 72 test points.

The remainder of this paper is organized as follows. Section II presents the system model of the considered RIS-assisted wireless communication system and clarifies the sensing objective. Section III discusses the challenges of using RIS for wireless signal sensing and presents an RIS-based sensing method under the constraint of passive reflection. Section IV designs a prototype system for sensing and positioning based on RIS, and analyzes the impact of non-ideal reflection coefficients. Section V implements the prototype system and provides experimental measurement results and positioning performance. Section VI concludes the paper.

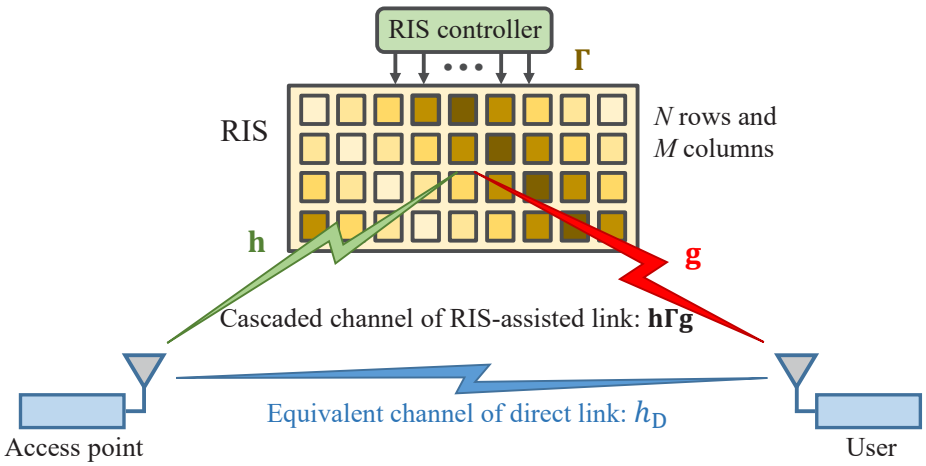

Fig. 1. The considered RIS-assisted wireless sensing and communication system.

II. System Model

We consider the RIS-assisted wireless communication system illustrated in Fig. 1, which consists of a single-antenna access point, a single-antenna user equipment, and an RIS composed of unit cells that are regularly distributed in N rows and M columns. In the considered system, the spatial dimension of the RIS is utilized to achieve wireless sensing and positioning. The wireless channel between the access point and the user can be written as

$$h_S = \sum_{m=1}^{M} \sum_{n=1}^{N} h_{n,m} \Gamma_{n,m} g_{n,m} + h_D, \tag{1}$$

where $h_{n,m}$, $\Gamma_{n,m}$, and $g_{n,m}$ denote the wireless channel between the access point and the unit cell $\mathrm{U_{n,m}}$ (i.e., the unit cell in the n^{th} row and m^{th} column), the reflection coefficient of $\mathrm{U_{n,m}}$, the wireless channel between $\mathrm{U_{n,m}}$ and the user, respectively. h_D denotes the equivalent wireless channel between the access point and the user that does not pass through the RIS.

Considering the uplink from the user to the access point, and the received signal of the access point is represented as

$$y(t) = h_S \sqrt{p} x e^{j2\pi f_c t} = \left(\sum_{m=1}^{M} \sum_{n=1}^{N} h_{n,m} \Gamma_{n,m} g_{n,m} + h_D \right) \sqrt{p} x e^{j2\pi f_c t}, \tag{2}$$

where p, x, and f_c denote the transmit power of the user, the transmitted symbol, and the carrier frequency, respectively. When considering the baseband model and the presence of noise, the

received baseband signal of the access point can be expressed as

$$y = h_S\sqrt{p}x + n = \left(\sum_{m=1}^{M}\sum_{n=1}^{N} h_{n,m}\Gamma_{n,m}g_{n,m} + h_D\right)\sqrt{p}x + w, \tag{3}$$

where w is the noise at the receiver of the access point. In this paper, based on the system model given in (3), we utilize the space-time coding capability of the RIS to design a scheme for sensing the wireless channel $g_{n,m}$ and enabling real-time positioning of the user based on RIS.

III. Wireless Signal Sensing Based on RIS

In wireless communication systems, the ability of network devices to sense wireless signals is indispensable, as it enables key foundational functions such as channel estimation, data reception, and spectrum cognition. In conventional wireless communication systems, the receiver is responsible for the sensing of wireless signals. In this section, we compare the hardware architecture and functional features of an RIS and a multichannel receiver, and then introduce an RIS-based method for wireless signal sensing.

A. Comparison of an RIS and a Multichannel Receiver

The hardware architecture of a multichannel receiver is shown in Fig.2(a), consisting of an antenna array and multiple receiving channels. Each receiving channel includes circuit modules such as filters, low noise amplifiers (LNA), mixers, local oscillators, analog-to-digital converters (ADC), and baseband processing units. When a wireless signal impinges on the antenna array, each antenna element in the array generates an induced current signal. These current signals, after entering the receiving channels connected to the antenna elements, undergo filtering, amplification, down-conversion, and analog-to-digital conversion, finally becoming processable baseband Rx signals.

The amplitude and phase of baseband received signals reflect the amplitude and phase of incident wireless signals, thereby enabling reception and processing of wireless signals. More importantly, the array structure of the antenna endows the receiver with the capability to sense the spatial dimension of wireless signals, which enables advanced communication technologies like MIMO transmission that utilize spatial dimension resources.

The hardware architecture of an RIS is shown in Fig.2(b). Compared to the multichannel receiver, the antenna array is replaced by an RIS array, and the receiving channels are substituted

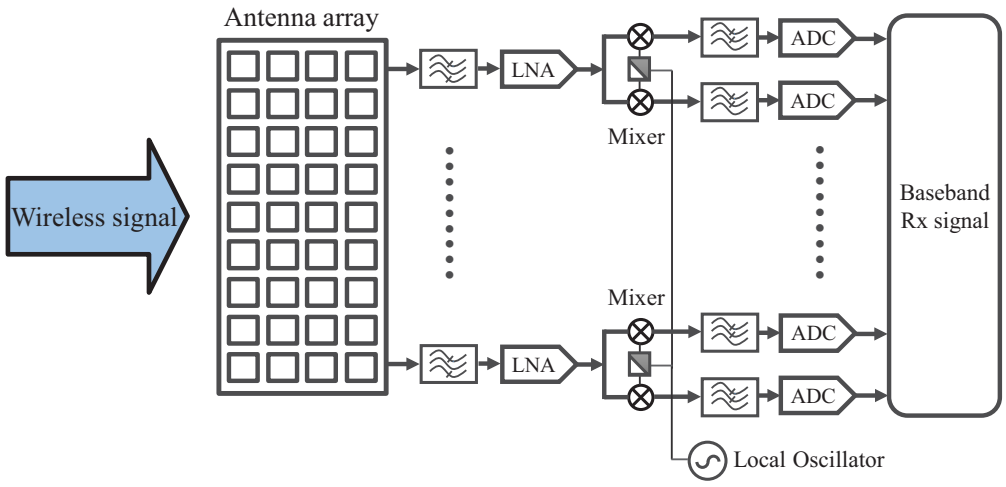

(a) A multichannel receiver

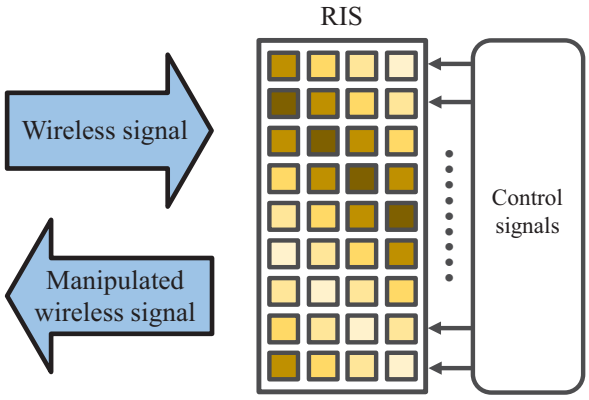

(b) An RIS

Fig. 2. Comparison of the hardware architecture and functionality between an RIS and a multichannel receiver.

with a feeding network of control signals. The capability to sense and receive wireless signals is transformed into the ability to directly manipulate them. On the one hand, as discussed in [21]–[23], the array structure of the RIS endows it with spatial coding capability, allowing the manipulation of wireless signals in the spatial domain. This also enables RIS-based MIMO transmitters, as realized in [24]. On the other hand, the hardware cost of an RIS is lower than that of a multichannel receivers with the same array size, as each channel of the receiver consists of expensive RF chains and baseband modules, while each channel of the RIS is made up of low-cost unit cells and control signal modules. Additionally, RIS offers the advantage of low power consumption [25].

Compared with multichannel receivers, RISs not only possess spatial dimension resources

but also have the advantages of low hardware cost and low power consumption. However, as indicated by its signal expression (3), since RIS can only perform adjustable passive reflection and usually cannot directly sense wireless signals, there is an urgent need to explore wireless signal sensing methods based on the RIS.

B. Design of Wireless Signal Sensing Function Under the Constraint of Passive Reflection

Based on the space-time-coding capability of RIS, the wireless signal sensing function is designed under the constraint of passive reflection. Specifically, consider the system shown in Fig.1. In the uplink transmission, the wireless signal incident on the unit cell $\mathrm{U_{n,m}}$ is

$$s_{n,m} = g_{n,m}\sqrt{p}x. \tag{4}$$

Therefore, the wireless signal incident on the RIS can be expressed as

$$\mathbf{s} = \mathbf{g}\sqrt{p}x, \tag{5}$$

where $\mathbf{s} = [s_{1,1}, s_{1,2}, \cdots, s_{1,M}, s_{2,1}, \cdots, s_{N,M}]^T \in \mathbb{C}^{NM\times 1}$ denotes the vector composed of wireless signals incident on each unit cell of the RIS, and $\mathbf{g} = [g_{1,1}, g_{1,2}, \cdots, g_{1,M}, g_{2,1}, \cdots, g_{N,M}]^T \in \mathbb{C}^{NM\times 1}$ denotes the channel vector between the single-antenna user and the RIS.

If the RIS is replaced by the antenna array of a multichannel receiver, the signal vector $\mathbf{s}$ could be directly obtained through the inherent wireless signal reception capability of the multichannel receiver, and thus directly estimate the channel vector $\mathbf{g}$. However, common RIS can only passively reflect incident wireless signals and cannot receive them (i.e. this work does not consider the concept of RIS hardware designs that combine active receiving elements with passive reflecting unit cells). In the following, we design a space-time coding matrix for the RIS and efficiently perform channel estimation for the channel vector $\mathbf{g}$ by only using the baseband received signal in (3) of the single-antenna access point , thereby enabling RIS-based wireless signal sensing.

In the RIS-assisted wireless communication system shown in Fig.1, the access point and the RIS are usually fixed in place, and the path between the access point and the RIS is primarily a quasi-static line-of-sight path. Therefore, it is assumed that the channel vector $\mathbf{h}$ between the access point and the RIS is static and known. During the process of estimating the channel vector $\mathbf{g}$, the user transmission symbol x is set to 1, which means the user transmits an unmodulated

carrier signal with a frequency f_c. The baseband received signal expression (3) at the access point can be further expressed as

$$y = \left(\sum_{m=1}^{M} \sum_{n=1}^{N} h_{n,m} \Gamma_{n,m} g_{n,m} + h_D \right) \sqrt{p} + w = \left(\mathbf{h} \mathbf{\Gamma} \mathbf{g} + h_D \right) \sqrt{p} + w, \tag{6}$$

where $\mathbf{h} = [h_{1,1}, h_{1,2}, \cdots, h_{1,M}, h_{2,1}, \cdots, h_{N,M}] \in \mathbb{C}^{1 \times NM}$ is the static and known channel vector between the access point and the RIS, and $\mathbf{\Gamma} = \operatorname{diag}\left\{ \mathit{\Gamma}_{1,1}, \mathit{\Gamma}_{1,2}, \cdots, \mathit{\Gamma}_{1,M}, \mathit{\Gamma}_{2,1}, \cdots, \mathit{\Gamma}_{N,M} \right\} \in {}^{NM \times NM}$ is the diagonal matrix composed of the reflection coefficients of the unit cells of the RIS.

The time-domain sequence design of the reflection coefficient for the unit cell $\mathrm{U_{n,m}}$ can be expressed as

$$\mathit{\Gamma}_{n,m}(t) = \sum_{q=1}^{Q} \mathit{\Gamma}_{n,m}^{q} R\left(t - (q-1) \frac{T_s}{Q} \right), \ t \in [0, T_s], \tag{7}$$

where

$$R(t) = \begin{cases} 1, & t \in [0, \frac{T_s}{Q}] \\ 0, & t \notin [0, \frac{T_s}{Q}] \end{cases} \tag{8}$$

is a rectangular window sampling function, $\mathit{\Gamma}_{n,m}^{q}$ is the q-th element of the sequence, Q is the total number of elements in the sequence, and T_s is the duration of the sequence, with each element lasting $\frac{T_s}{Q}$.

Theorem 1: Assume that the duration T_s of the sequence is shorter than the channel coherence time, and let each unit cell of the RIS execute the time-domain sequence of reflection coefficient as defined by equation (7), the l-th order harmonic component of the received signal of the access point is given by

$$Y_l = \sum_{m=1}^{M} \sum_{n=1}^{N} h_{n,m} a_{n,m}^{l} g_{n,m} \sqrt{p} + W_l = \mathbf{h} \mathbf{A}_l \mathbf{g} \sqrt{p} + W_l, \tag{9}$$

where W_l denotes the received noise at the l-th order harmonic, and the matrix $\mathbf{A}_l$ is defined as

$$\mathbf{A}_l = \operatorname{diag}\left\{ a_{1,1}^{l}, a_{1,2}^{l}, \cdots, a_{1,M}^{l}, a_{2,1}^{l}, \cdots, a_{N,M}^{l} \right\} \in \mathbb{C}^{NM \times NM}, \tag{10}$$

and the element in $\mathbf{A}_l$ is

$$a_{n,m}^{l} = \frac{T_s}{Q} \operatorname{sinc}\left(\frac{\pi l}{Q} \right) \sum_{q=1}^{Q} \mathit{\Gamma}_{n,m}^{q} e^{-j\pi \frac{2q-1}{Q} l}, \tag{11}$$

which is the l-th order harmonic component of the time-domain sequence of the reflection coefficient for the unit cell $\mathrm{U_{n,m}}$.

Proof: See Appendix A. ■

Theorem 1 indicates that the l-th order harmonic component of the signal received by the access point is the sum of the l-th order harmonic components generated by each unit cell on its respective auxiliary reflection path. This offers an effective approach for mapping the spatial dimension of the RIS to the frequency domain. Furthermore, as observed from equation (9), the l-th order harmonic component of the signal received by the access point is not affected by the equivalent channel h_D of the direct link (i.e., the equivalent channel without passing through the RIS). This is because h_D is a non-adjustable conventional channel, lacking the space-time coding capability of the RIS and, therefore, cannot actively generate harmonic signals. This is a very beneficial property, as it fundamentally avoids the impact of the direct link when estimating the channel vector $\mathbf{g}$, which is advantageous for realizing RIS-based wireless signal sensing functionality.

The channel vector $\mathbf{g}$ between the user and the RIS contains $N \times M$ unknown elements. Therefore, $N \times M$ harmonic components of the received signal of the access point are selected to form the observation vector, which is expressed as

$$\mathbf{y} = [Y_{l_1}, Y_{l_2}, \cdots, Y_{l_{NM}}]^T \in \mathbb{C}^{NM\times 1}, \tag{12}$$

where Y_{l_k} represents the k-th harmonic component of the received signal of the access point, and the harmonic is of the l_k-th order. According to equation (9), the observation vector shown in equation (12) can be expressed as

$$\mathbf{y} = \sqrt{p}\mathbf{U}\mathbf{g} + \mathbf{w}, \tag{13}$$

where $\mathbf{U} = [\mathbf{h}\mathbf{A}_{l_1}, \mathbf{h}\mathbf{A}_{l_2}, \cdots, \mathbf{h}\mathbf{A}_{l_{NM}}]^T \in \mathbb{C}^{NM\times NM}$ is a known matrix that can be freely designed, and $\mathbf{w} = [W_{l_1}, W_{l_2}, \cdots, W_{l_{NM}}]^T \in \mathbb{C}^{NM\times 1}$ is the noise vector at the access point. Based on equation (13), the least squares estimation of the channel vector $\mathbf{g}$ between the user and the RIS can be obtained as

$$\widetilde{\mathbf{g}} = \frac{\mathbf{U}^{-1}}{\sqrt{p}}\mathbf{y} = \mathbf{g} + \frac{\mathbf{U}^{-1}\mathbf{w}}{\sqrt{p}}, \tag{14}$$

where $\widetilde{\mathbf{g}}$ is the estimated value of the channel $\mathbf{g}$, and $\mathbf{U}^{-1}$ represents the inverse of matrix $\mathbf{U}$.

It is worth noting that although the inversion of matrix $\mathbf{U}$ is required when estimating $\mathbf{g}$, once the time-domain sequence in equation (7) is designed, matrix $\mathbf{U}$ remains fixed. Therefore, when performing continuous estimations of $\mathbf{g}$, the inverse of matrix $\mathbf{U}$ only needs to be computed initially, without the need for repeated inversion in each estimation. Consequently, the proposed

method for sensing wireless signals (estimating the channel vector $\mathbf{g}$ of the incident path) based on the space-time-coding capability of the RIS is highly efficient. Moreover, as validated in [26], common RISs are reciprocal. Thus, the above method is also applicable to the downlink transmission of RIS-assisted wireless communication systems, by swapping the roles of the access point and the user in terms of transmission and reception.

IV. Design and Analysis of an RIS-based Positioning Prototype System

A positioning prototype system is designed to validate the RIS-based wireless signal sensing method proposed in the previous section. This section first presents the architecture of the prototype system and the scheme of positioning based on AoAs. Then, it introduces the method for estimating the AoA on the RIS, followed by an analysis demonstrating that the proposed method is robust against the non-ideal characteristics of the RIS hardware. Finally, the design of the wireless frame is provided.

A. Prototype System Architecture and Positioning Scheme

The block diagram of the RIS-based sensing and positioning prototype system is shown in Fig. 3. The prototype system includes a single-antenna user, a dual-antenna access point, and two RIS panels. Without loss of generality, we consider the uplink scenario. The access point collaborates with the two RIS panels using the method designed in the previous section. By leveraging the spatial dimension of the RIS, the system senses the wireless signals transmitted by the user and calculates the angles of arrival from the user to the two RIS panels, subsequently estimating the position of the user.

Both RIS panels are designed identically and feature column-controlled structures, thereby functioning as two uniform linear array RISs with adjustable reflection capabilities. Hence, the two-dimensional positioning prototype system, as shown in Fig. 3, is constructed to locate the user in the x–o–y plane. The user's transmitting antenna, the center points of the two RIS panels, and the two receiving antennas of the access point are all at the same height ($z = 0$). The surfaces of the two RIS panels are perpendicular to the ground, with their central normal lines directly pointing toward the two receiving antennas of the access point via the line-of-sight paths, respectively. Both receiving antennas are in the far-field region of the RIS panels. This setup ensures that the channels from the unit cells of RIS 1 to receiving antenna 1 are the same, thereby enabling the easy obtaining of channel vector $\mathbf{h_1}$. This facilitates the implementation

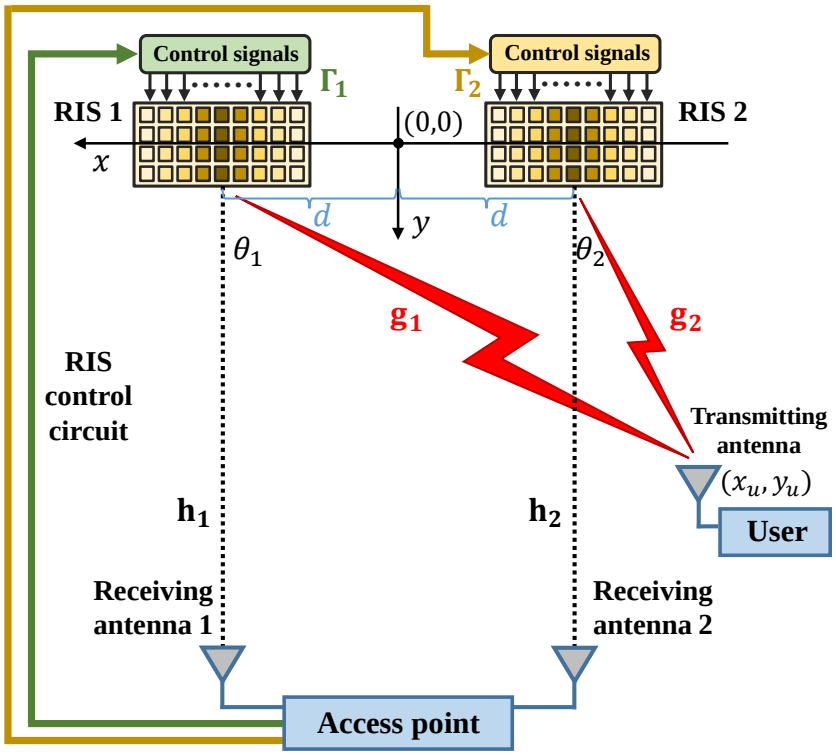

Fig. 3. The block diagram of the RIS-based sensing and positioning prototype system.

of the RIS-based wireless signal sensing method designed in the previous section. The same considerations apply to RIS 2 and receiving antenna 2.

After estimating the wireless channels $\mathbf{g_1}$ and $\mathbf{g_2}$ shown in Fig. 3 by using the RIS-based wireless signal sensing method designed in Section III, $\mathbf{g_1}$ and $\mathbf{g_2}$ can be transformed into spatial domain sampled data through Fourier transform to estimate the angles of arrival θ_1 and θ_2. In the coordinate system shown in Fig. 3, the center points of RIS 1 and RIS 2 are located at $(-d, 0)$ and $(d, 0)$ respectively. Based on geometric relationships, the x-coordinate of the user can be calculated as

$$x_u = d - \frac{2d\ \sin\theta_1 \cos\theta_2}{\sin(\theta_1 - \theta_2)}, \tag{15}$$

and the y-coordinate of the user can be calculated as

$$y_u = \frac{2d\ \cos\theta_1 \cos\theta_2}{\sin(\theta_1 - \theta_2)}. \tag{16}$$

B. Estimation Method of the AoA of RIS

This subsection focuses on designing a specific AoA estimation method by using the 27 GHz millimeter-wave RIS illustrated in Fig. 4. This millimeter-wave RIS is a column-controlled struc-

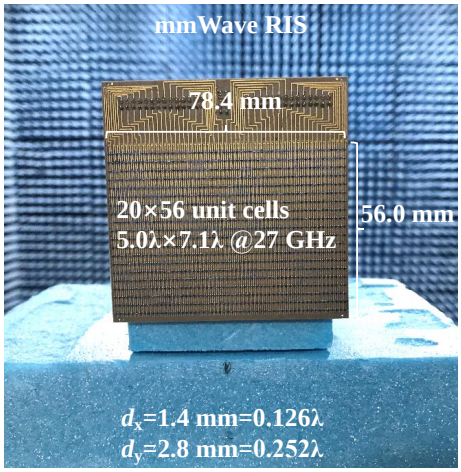

Fig. 4. The photograph of the utilized millimeter-wave RIS.

ture with 56 columns and 20 rows of unit cells, where each column supports 1-bit reflective phase control [27]. Due to the utilized RIS controller outputs 48 digital control signals simultaneously, thus only the 48 columns in the middle of the 56 columns are actually controlled. Considering that the width of each single column is only $0.126\,\lambda$, and to reduce control complexity for rapid prototyping, every 3 columns are grouped into one macro cell. Each macro cell consists of 20 rows and 3 columns of unit cells, as shown in Fig. 5, forming a total of 16 macro cells.

Each macro cell, which consists of three columns of unit cells, is controlled by a time-domain coding sequence. The ideal reflection coefficient of the 1-bit phase-adjustable macro cell can be expressed as

$$\Gamma_v = \begin{cases} A, & \text{coding } \text{“1”} \\ -A, & \text{coding } \text{“0”} \end{cases}, \tag{17}$$

where $v \in [1, 16]$ is the index of the macro cell, A is the amplitude component of the reflection coefficient, and the two coding states correspond to phase components of 0° and 180°, respectively.

Let Γ_v^q represent the q-th element of the time-domain coding sequence of the reflection coefficient for the v-th macro cell. As shown in Fig. 5, the elements of the time-domain coding sequence of the first macro cell are designed as

$$\Gamma_1^q = \begin{cases} A, & q \in [1, 16] \\ -A, & q \in [17, 32] \end{cases}. \tag{18}$$

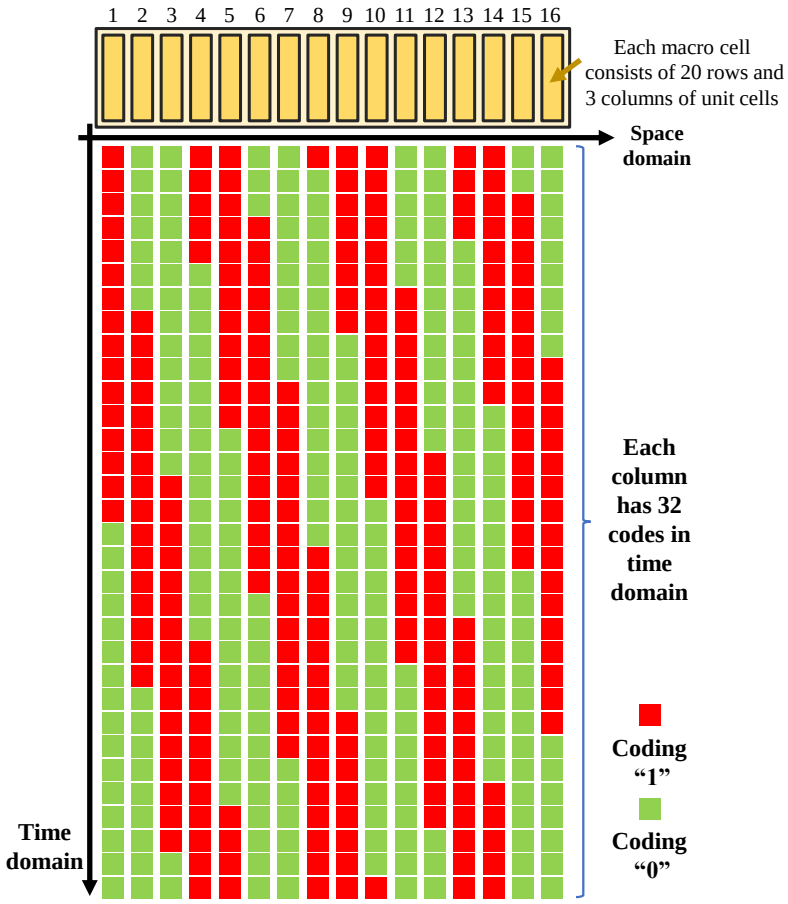

Fig. 5. The designed space-time coding matrix of the reflection coefficients of the 16 macro cells.

According to equation (7), the corresponding time-domain sequence of the reflection coefficient can be represented as

$$\Gamma_1(t) = \sum_{q=1}^{32} \Gamma_1^q R\left(t - (q-1)\frac{T_s}{32}\right), t \in [0, T_s]. \tag{19}$$

Based on equation (11) from Theorem 1, the l-th order harmonic component of the time-domain

sequence of the reflection coefficient for the first macro cell, as shown in equation (19), is

$$\begin{aligned} a_1^l &= \frac{T_s}{32}\mathrm{sinc}(\frac{\pi l}{32})\sum_{q=1}^{32}\Gamma_1^q e^{-j\pi\frac{2q-1}{32}l} \\ &= \frac{T_s}{\pi l}\sin(\frac{\pi l}{32})\left[A\sum_{q=1}^{16}e^{-j\pi\frac{2q-1}{32}l} - A\sum_{q=17}^{32}e^{-j\pi\frac{2q-1}{32}l}\right] \\ &= \frac{T_s}{\pi l}\sin\left(\frac{\pi l}{32}\right)e^{j\frac{\pi l}{32}}A\left(e^{-j\frac{1}{16}\pi l} - e^{-j\frac{17}{16}\pi l}\right)\left(\frac{1-e^{-j\pi l}}{1-e^{-j\frac{\pi l}{16}}}\right) \\ &= \frac{T_s A}{2j\pi l}\left(e^{j\frac{\pi l}{32}} - e^{-j\frac{\pi l}{32}}\right)e^{j\frac{\pi l}{32}}\left(1-e^{-j\pi l}\right)^2 e^{-j\frac{1}{16}\pi l}\left(\frac{1}{1-e^{-j\frac{\pi l}{16}}}\right) \\ &= \frac{T_s A}{2j\pi l}\left(1-e^{-j\pi l}\right)^2 \\ &= \frac{-2jT_s A}{\pi l}\sin^2(\frac{\pi l}{2}) \end{aligned} \tag{20}$$

As illustrated in Fig. 5, the time-domain sequence of the reflection coefficient for the first macro cell is cyclically shifted by $7(v-1)$ elements to obtain the time-domain sequence of the reflection coefficient for the v-th macro cell. According to the time-shifting property of the Fourier transform, the l-th order harmonic component of the time-domain sequence of the reflection coefficient for the v-th macro cell is

$$\begin{aligned} a_v^l &= \frac{-2jT_s A}{\pi l}\sin^2(\frac{\pi l}{2})e^{-j\frac{2\pi}{T_s}l\cdot\frac{7}{32}(v-1)T_s} \\ &= \frac{-2jT_s A}{\pi l}\sin^2(\frac{\pi l}{2})e^{-j\frac{7}{16}(v-1)\pi l}. \end{aligned} \tag{21}$$

Using equations (21) and (10), the matrix $\mathbf{U}$ in equation (13) can be constructed, thereby enabling the estimation for the channel vector $\mathbf{g}$ from the user to the RIS by using equation (14), achieving RIS-based wireless signal sensing.

Since the RIS is divided into 16 macro cells, there are a total of 16 sub-channels between the user and the RIS, meaning that the channel vector $\mathbf{g}$ consists of 16 unknown elements to be solved. Therefore, 16 harmonic components of the received signal at the access point need to be selected as the observation vector. As shown in equation (21), the even-order harmonic components of the designed time-domain sequence are always 0. Hence, 16 odd-order harmonic components between the -15th and +15th order harmonics of the received signal at the access point are selected to form the observation vector $\mathbf{y}$.

On the other hand, as shown in Fig. 3, the receiving antenna is located directly in front of the corresponding RIS along the line-of-sight path and is in the far-field region of the RIS. Therefore, the channel vector $\mathbf{h}$ between the RIS and the corresponding receiving antenna is

dominated by the stationary line-of-sight path and the elements in $\mathbf{h}$ are the same. $\mathbf{h}$ can be written as

$$\mathbf{h} = [\beta, \cdots, \beta, \cdots, \beta] \in \mathbb{C}^{1\times 16}, \tag{22}$$

where β represents the channel between each macro cell of the RIS and the receiving antenna directly in front of it. Since the RIS and the access point are fixed, β can be regarded as a complex constant within the system.

Because 16 odd-order harmonic components between the -15th and the +15th order harmonics of the signal received by the access point are selected as the observation vector, according to equations (13), (21) and (22), the expressions for these 16 harmonic components of the received signal is given as

$$\begin{aligned}
\begin{bmatrix} Y_{-15} \\ Y_{-13} \\ \vdots \\ Y_{-1} \\ Y_{1} \\ \vdots \\ Y_{13} \\ Y_{15} \end{bmatrix} &= \sqrt{p}\beta \begin{bmatrix} a_1^{-15} & a_2^{-15} & \cdots & a_{16}^{-15} \\ a_1^{-13} & a_2^{-13} & \cdots & a_{16}^{-13} \\ \vdots & \vdots & \ddots & \vdots \\ a_1^{-1} & a_2^{-1} & \cdots & a_{16}^{-1} \\ a_1^{1} & a_2^{1} & \cdots & a_{16}^{1} \\ \vdots & \vdots & \ddots & \vdots \\ a_1^{13} & a_2^{13} & \cdots & a_{16}^{13} \\ a_1^{15} & a_2^{15} & \cdots & a_{16}^{15} \end{bmatrix} \begin{bmatrix} g_1 \\ g_2 \\ \vdots \\ g_{16} \end{bmatrix} + \begin{bmatrix} W_{-15} \\ W_{-13} \\ \vdots \\ W_{-1} \\ W_{1} \\ \vdots \\ W_{13} \\ W_{15} \end{bmatrix} \\
&= \sqrt{p}\beta \frac{-2jT_sA}{\pi} \begin{bmatrix} c_1^{-15} & c_2^{-15} & \cdots & c_{16}^{-15} \\ c_1^{-13} & c_2^{-13} & \cdots & c_{16}^{-13} \\ \vdots & \vdots & \ddots & \vdots \\ c_1^{-1} & c_2^{-1} & \cdots & c_{16}^{-1} \\ c_1^{1} & c_2^{1} & \cdots & c_{16}^{1} \\ \vdots & \vdots & \ddots & \vdots \\ c_1^{13} & c_2^{13} & \cdots & c_{16}^{13} \\ c_1^{15} & c_2^{15} & \cdots & c_{16}^{15} \end{bmatrix} \begin{bmatrix} g_1 \\ g_2 \\ \vdots \\ g_{16} \end{bmatrix} + \begin{bmatrix} W_{-15} \\ W_{-13} \\ \vdots \\ W_{-1} \\ W_{1} \\ \vdots \\ W_{13} \\ W_{15} \end{bmatrix},
\end{aligned} \tag{23}$$

where

$$c_v^l = \frac{1}{l}\sin^2(\frac{\pi l}{2})e^{-j\frac{7}{16}(v-1)\pi l}. \tag{24}$$

The expression in equation (23) is rewritten in matrix form

$$\mathbf{y} = \frac{-2j\sqrt{p}T_sA\beta}{\pi}\mathbf{C}\mathbf{g} + \mathbf{w}, \tag{25}$$

where $\mathbf{C}$ is a known constant matrix composed of 16 rows and 16 columns of elements c_v^l, as shown in equation (23). The inverse matrix $\mathbf{C^{-1}}$ exists and is also a known constant matrix. According to equation (25), by simply multiplying the constant matrix $\mathbf{C^{-1}}$ by the observation vector $\mathbf{y}$, we obtain

$$\widetilde{\mathbf{g}'} = \mathbf{C}^{-1}\mathbf{y} = \frac{-2j\sqrt{p}T_s A\beta}{\pi}\mathbf{g} + \mathbf{C}^{-1}\mathbf{w}, \tag{26}$$

where $\widetilde{\mathbf{g}'}$ represents the estimated result of the channel vector $\mathbf{g}$ between the user and the RIS, after being multiplied by several constant terms. As indicated in equation (26), the larger these constant terms are, the higher the signal-to-noise ratio (SNR) of the estimation result. That is, the higher the user's transmit power p, the longer the sequence duration T_s (which must be less than the channel coherence time), the higher the amplitude component (reflection efficiency) A of the reflection coefficient, and the larger the channel gain $|\beta|$ between the macro cell and the receiving antenna, the more accurate the estimate will be, which aligns with intuition.

The 16 macro cells of the RIS form a one-dimensional linear array. Therefore, performing a Discrete Fourier Transform (DFT) on the estimated channel vector $\widetilde{\mathbf{g}'}$ yields spatial domain sampling data

$$F_{RIS}(\theta) = \sum_{v=1}^{16} F(\theta)\widetilde{g'}_v e^{j(v-1)k_0 D sin\theta}, \tag{27}$$

where $F(\theta)$ represents the scattering pattern of each macro cell. Based on the measurement results in [27], we set $F(\theta) = \sqrt{cos\theta}$ here. $\widetilde{g'}_v$ denotes the v-th element of $\widetilde{\mathbf{g}'}$, $k_0 = \frac{2\pi f_c}{c}$is the wavenumber, and D is the distance between the centers of adjacent macro cells.

In the prototype system design shown in Fig. 3, the estimated value of the AOA for the signal transmitted by the user to each RIS can be obtained as

$$\widetilde{\theta} = \arg\max_{\theta} F_{RIS}(\theta). \tag{28}$$

Based on equation (28), the AoAs $\widetilde{\theta}_1$ and $\widetilde{\theta}_2$ of the user's transmitted signal to the two RIS panels can be obtained in the prototype system, respectively. By substituting the estimated AoAs into equations (15) and (16), the user's position coordinates $(\widetilde{x}_u, \widetilde{y}_u)$ can be determined, thereby achieving the RIS-based positioning function.

C. Analysis of the Impact of Non-Ideal Reflection Coefficients

In the design process of the previous subsection, it was assumed that the 1-bit phase-adjustable reflection coefficient is perfectly ideal, as shown in equation (17). That is, the reflection amplitudes of the RIS unit cells are exactly the same for coding "0" and coding "1", with the reflection

phases differing by exactly 180 degrees. However, in practice, the reflection coefficients of the unit cells often have different amplitude responses for "0" and "1" codings, and the phase shift is often not exactly opposite. Some research findings reveal that the reflection coefficients even depend on the angles of incidence/observation [28]–[30].

Therefore, by considering a more general and practical situation, the reflection coefficient of the 1-bit adjustable macro cell can be expressed as

$$\Gamma_v = \begin{cases} A_0 e^{j\varphi_0}, & \text{coding "1"} \\ A_1 e^{j\varphi_1}, & \text{coding "0"} \end{cases}. \tag{29}$$

At this point, the elements of the designed time-domain coding sequence of the first macro cell, i.e., equation (18), should be rewritten as

$$\Gamma_1^q = \begin{cases} A_0 e^{j\varphi_0}, & q \in [1, 16] \\ A_1 e^{j\varphi_1}, & q \in [17, 32] \end{cases}. \tag{30}$$

Substituting equation (30) into equation (19), the l-th order harmonic component of the time-domain reflection coefficient sequence for the first macro cell is given by

$$\begin{aligned} a_1^l &= \frac{T_s}{32}\text{sinc}(\frac{\pi l}{32})\sum_{q=1}^{32}\Gamma_1^q e^{-j\pi\frac{2q-1}{32}l} \\ &= \frac{T_s}{\pi l}\sin(\frac{\pi l}{32})\left[A_0 e^{j\varphi_0}\sum_{q=1}^{16}e^{-j\pi\frac{2q-1}{32}l} + A_1 e^{j\varphi_1}\sum_{q=17}^{32}e^{-j\pi\frac{2q-1}{32}l}\right] \\ &= \frac{T_s}{2j\pi l}\left(A_0 e^{j\varphi_0} + A_1 e^{j\varphi_1}e^{-j\pi l}\right)\left(1 - e^{-j\pi l}\right) \\ &= \frac{-jT_s\left(A_0 e^{j\varphi_0} - A_1 e^{j\varphi_1}\right)}{\pi l}\sin^2(\frac{\pi l}{2}). \end{aligned} \tag{31}$$

Considering the practical reflection coefficient characteristics of the RIS, based on equation (31) and the time-shift property of the Fourier transform, the l-th order harmonic component of the time-domain reflection coefficient sequence for the v-th macro cell is

$$a_v^l = \frac{-jT_s\left(A_0 e^{j\varphi_0} - A_1 e^{j\varphi_1}\right)}{\pi l}\sin^2(\frac{\pi l}{2})e^{-j\frac{7}{16}(v-1)\pi l}. \tag{32}$$

Comparing equation (21) and equation (32), it can be observed that they differ only in the constant terms $2A$ and $(A_0 e^{j\varphi_0} - A_1 e^{j\varphi_1})$, with the former being a special case of the latter. By substituting equation (32) into equation (23) and estimating the channel $\mathbf{g}$ using the method designed in the previous subsection, we obtain

$$\widetilde{\mathbf{g}''} = \mathbf{C}^{-1}\mathbf{y} = \frac{-j\sqrt{p}T_s\left(A_0 e^{j\varphi_0} - A_1 e^{j\varphi_1}\right)\beta}{\pi}\mathbf{g} + \mathbf{C}^{-1}\mathbf{w}. \tag{33}$$

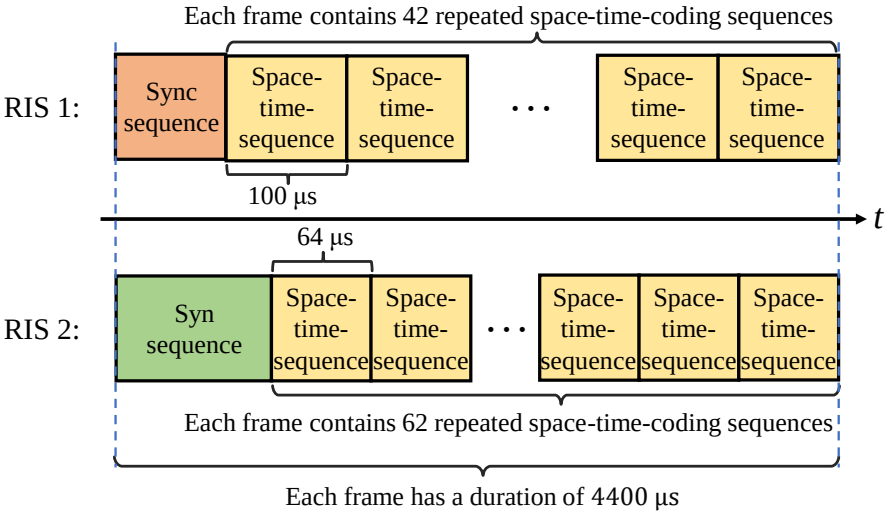

Fig. 6. The wireless frame structure of the prototype system.

Comparing equation (26) and equation (33), it can be observed that, even when considering the practical reflection coefficient characteristics of the RIS hardware, the constant matrix $\mathbf{C}^{-1}$, which is multiplied on the left side of the observation vector $\mathbf{y}$ to estimate the channel $\mathbf{g}$, remains unchanged. This indicates that the designed method is still feasible and it is robust against the non-ideal characteristics of the RIS reflection coefficients.

The practical reflection coefficient characteristics of the RIS do not affect the implementation of RIS-based wireless signal sensing function, only impacting the SNR of the estimation results. If the amplitude component of the ideal reflection coefficient of the unit cell is set to $A = 1$, then the non-ideal reflection coefficient characteristics would cause a reduction in the SNR (in dB) of the estimated channel vector $\mathbf{g}$ by

$$\eta = 10\log\left(\frac{2A}{A_0 e^{j\varphi_0} - A_1 e^{j\varphi_1}}\right) = 10\log\left(\frac{2}{A_0 e^{j\varphi_0} - A_1 e^{j\varphi_1}}\right). \tag{34}$$

D. Design of the Wireless Frame Structure for the Prototype System

The block diagram of the prototype system is shown in Fig. 3. During the execution of the user positioning function, the user transmits a 27 GHz single-tone carrier signal. The two RIS panels and their respective single-antenna receivers at the access point execute the designed RIS-based AoA estimation method. After estimating the AoAs θ_1 and θ_2, the user's position coordinates can be calculated based on geometric relationships, thus realizing the positioning function.

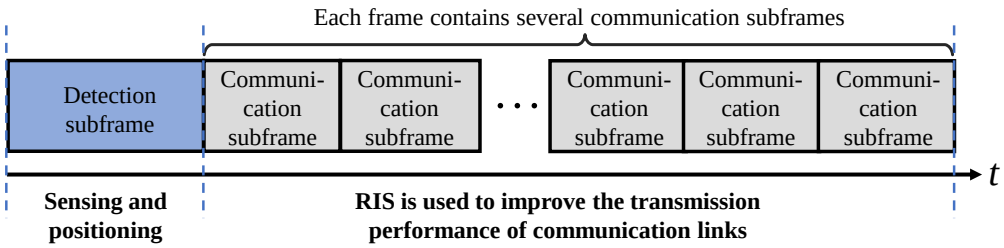

Fig. 7. A form of complete wireless frame structure

In order to ensure that the AoA estimation processes for the two RIS panels do not interfere with each other, it is necessary to guarantee that their observation vectors $\mathbf{y}$ are orthogonal. One method to achieve this is time-domain orthogonality, where AoA estimation for RIS 1 is performed first, followed by AoA estimation for RIS 2. This completes one positioning process but is inefficient and increases time overhead. Another approach is frequency-domain orthogonality, where both RISs simultaneously perform AoA estimation, and the 16 harmonic components of their observation vectors $\mathbf{y}$ are separated in the frequency domain, avoiding mutual interference.

The prototype system adopts the frequency-domain orthogonality approach. The wireless frame structure designed for prototype validation is shown in Fig. 6. Each of the two RIS panels modulates the incident single-tone carrier signal from the user according to its respective frame structure, adding synchronization sequences and space-time-coding sequences to the reflected signals. The space-time coding matrix of the reflection coefficients of RIS 1 and RIS 2 follow the design outlined in Fig. 5. The only difference is that the space-time sequence duration for RIS 1 is T_s = 100 μs, while it is T_s = 64 μs for RIS 2. As a result, the 16 odd-order harmonic frequency points generated by RIS 1 within the range of -15th to +15th harmonics are $\{-150, -130, \cdots, -10, 10, \cdots, 130, 150\}$kHz + 27 GHz. For RIS 2, the corresponding harmonic frequency points are $\{-234.375, -203.125, \cdots, -15.625, 15.625, \cdots, 203.125, 234.375\}$kHz + 27 GHz. These frequency points do not overlap, preventing spectral aliasing between the reflected signals generated by the two RISs. This ensures that the prototype system can successfully estimate the AoAs θ_1 and θ_2 simultaneously, thus obtaining the user's position coordinates.

It is worth noting that the purpose of the above wireless frame structure design for the prototype system is to enable rapid validation of the RIS-based wireless signal sensing and positioning functions, using experimental measurement results to verify the proposed system architecture

and method.

As shown in Fig. 7, in an RIS-assisted wireless communication system, this can be incorporated as a detection subframe within a complete wireless frame structure to obtain user location information. During the detection subframe, the RIS performs sensing and positioning functions. Following the detection subframe are several communication subframes, where the RIS utilizes the user's location information to perform functions such as beam tracking to enhance the performance of communication links.

V. Implementation and Measurement of an RIS-based Positioning Prototype System

This section introduces the physical implementation of the RIS-based sensing and positioning prototype system, illustrating the hardware architecture and the roles of each hardware module within the system. The constructed prototype system employs two 27 GHz RIS panels to achieve AoA estimation and positioning functions. The experimental measurement results verify the feasibility of the proposed RIS-based wireless signal sensing method and positioning system architecture.

A. Prototype System Setup

As shown in Fig. 8, we employ a millimeter-wave signal generator, two millimeter-wave RIS panels, two millimeter-wave front-ends, a software defined radio (SDR) platform, antennas, and several PXIe modules to implement the prototype system as follows.

(1) Millimeter-wave signal generator: the millimeter-wave signal generator produces a 27 GHz single-tone RF signal to the horn antenna as the user's transmission signal incident on the RIS.

(2) Millimeter-wave RIS: the utilized RIS can operate at 27 GHz as depicted in Fig. 4. It consists of 56 columns and 20 rows of unit cells. External digital control signals can change the state of the PIN diodes on the unit cells to achieve 1-bit reflection phase control. Detailed parameters can be found in [27]. Two of this kind RIS are used in the prototype system, each divided into 16 macro cells for control, as described in the previous section.

(3) FPGA digital output module: the FPGA digital output module contains 48 digital channels with a maximum sampling rate of 100 MSa/s. It maps the space-time-coding matrix as shown in Fig. 5 into corresponding digital high-low level signal sequences. After framing the sequences according to the wireless frame structure shown in Fig. 6, it outputs the digital signal sequences

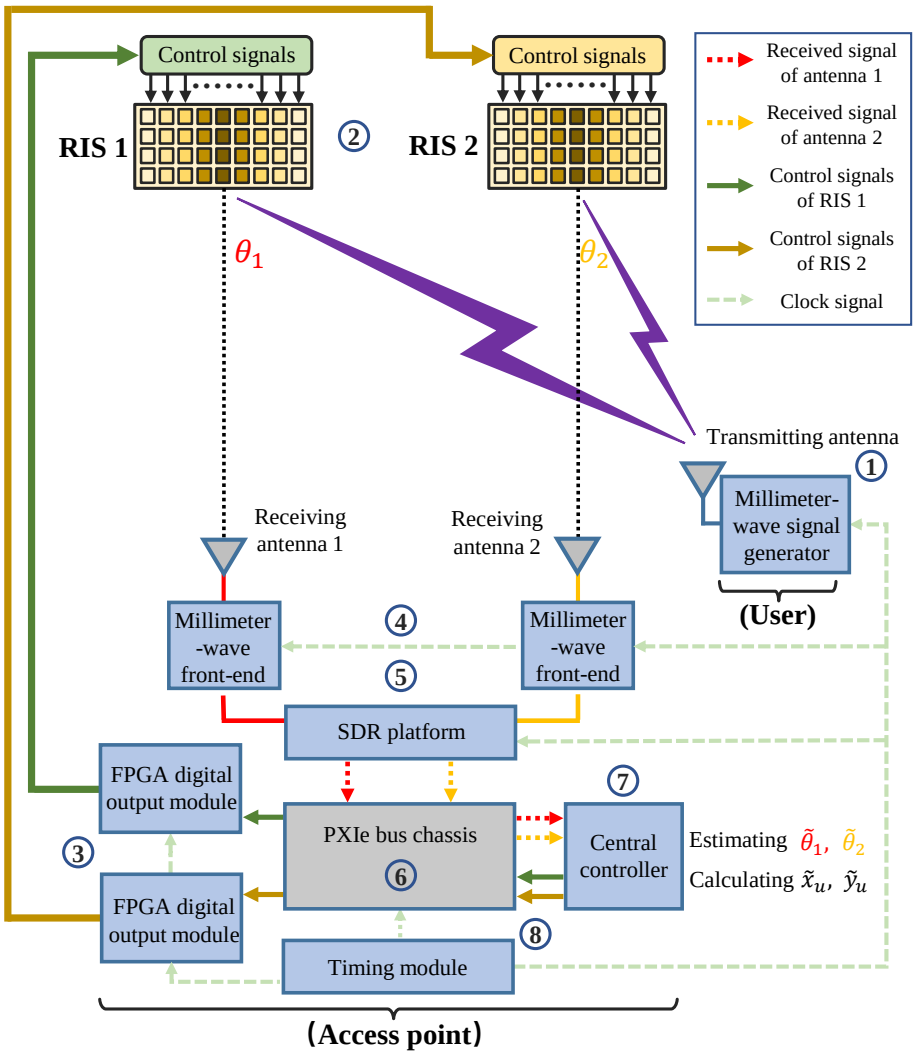

Fig. 8. The hardware architecture of the RIS-based sensing and positioning prototype system.

to the RIS. The prototype system contains two FPGA digital output modules, each providing control signals to one RIS.

(4) Millimeter-wave front-end: the millimeter-wave front-end downconverts the received 27 GHz signals to 1.8 GHz intermediate frequency (IF) signals, which are then provided to the SDR platform for reception and processing. The prototype system contains two millimeter-wave front-ends, each connected to one of the two receiving channels of the SDR platform.

(5) SDR platform: the SDR platform has two receiving channels that further downconvert the 1.8 GHz IF signals to baseband signals. These digital baseband signals are then transmitted to the central controller for further processing.

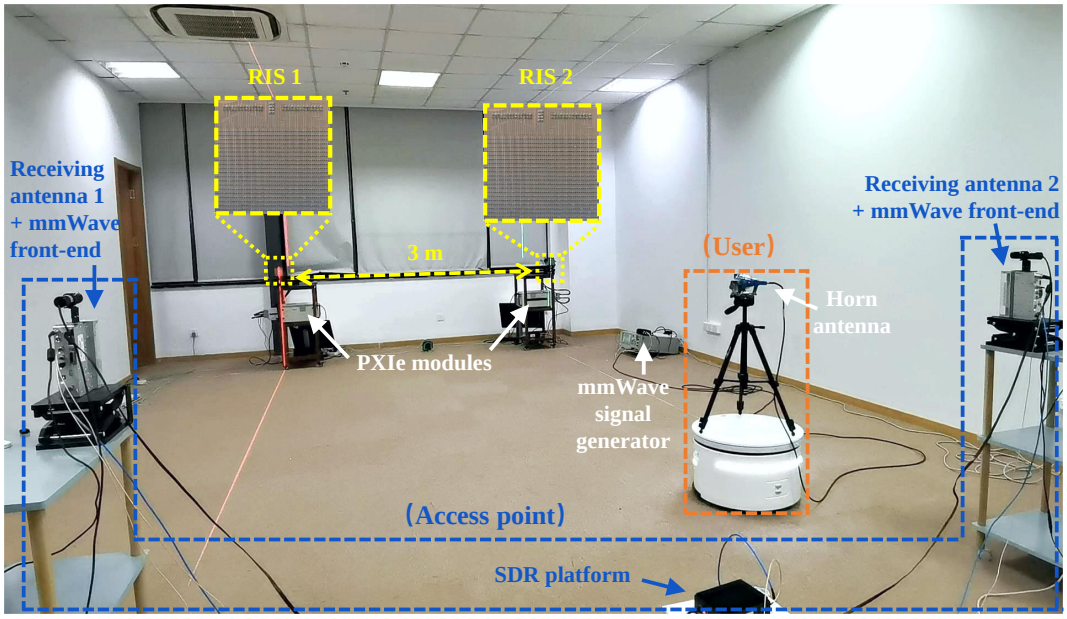

Fig. 9. The photograph of the RIS-based sensing and positioning prototype system.

(6) PXIe bus chassis: the PXIe bus chassis provides a high-speed bus interface for data and control exchanges between the central controller and peripheral hardware modules.

(7) Central controller: the central controller integrates the development environment for the prototype system, where the host program and FPGA program are developed to generate the space-time-coding matrix and wireless frame structure for the two RIS control signals, which are then sent to the FPGA digital output modules. Additionally, the central controller performs spectral analysis on the two received digital baseband signals to obtain observation vectors composed of 16 odd-order harmonic components. It then executes the designed method to estimate the AoAs $\widetilde{\theta}_1$ and $\widetilde{\theta}_2$ for the two RISs, and subsequently calculates the user's position coordinates $(\widetilde{x}_u, \widetilde{y}_u)$.

(8) Timing module: the timing module provides a common 10 MHz reference clock to all hardware modules.

As shown in the upper part of Fig. 8, the user equipment in the prototype system consists of a transmitting antenna and a millimeter-wave signal generator, which continuously transmits a 27 GHz signal to the two RIS panels. The RIS panels perform space-time-coding modulation on the incident wireless signals and reflect them. The reflected signals are received by two receiving antennas. As shown in the lower part of Fig. 8, the access point in the prototype system is composed of two receiving antennas, millimeter-wave front-ends, an SDR platform,

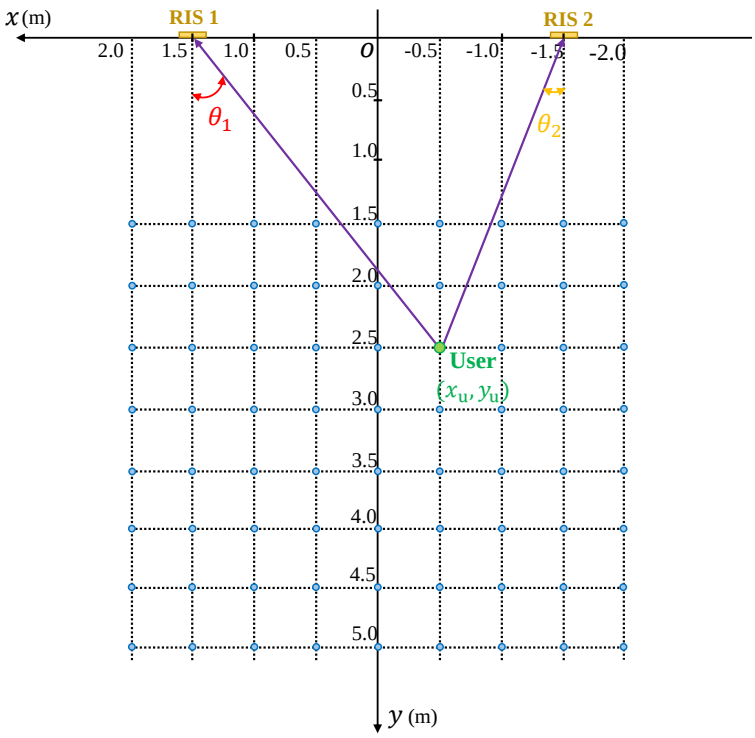

Fig. 10. The coordinates of the test points.

and a PXIe system equipped with various modular instruments. On one hand, it generates the control signal sequences required by the RIS panels, and on the other hand, it analyzes and processes the signals modulated and reflected by the RIS panels to achieve AoA estimation and user positioning functions.

B. Experimental Results

The RIS-based sensing and positioning prototype system is shown in Fig. 9. Two 27 GHz millimeter-wave RIS panels are located in the center of the figure, with a distance of 3 meters between each other, and an enlarged view is provided above. On the right part of the figure is the user, consisting of a horn antenna and a millimeter-wave signal generator, which emits a 27 GHz RF signal toward RIS panels. The access point is located at the bottom of the figure, receiving the reflected signals from the two RIS panels to estimate the AoAs and the user's position. As described in the previous section, the RIS panels adopt a column-controlled structure. Therefore, two RIS panels are utilized to achieve two-dimensional positioning on the horizontal plane.

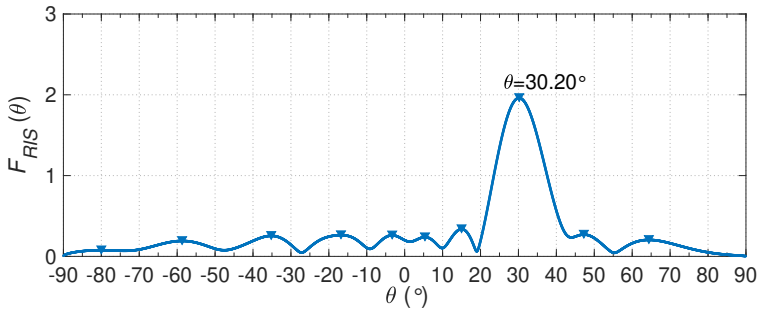

(a) The measured beamspace domain of the incident wireless signal on RIS 1 when the user is located at $(-0.5\,\mathrm{m}, 3.5\,\mathrm{m})$

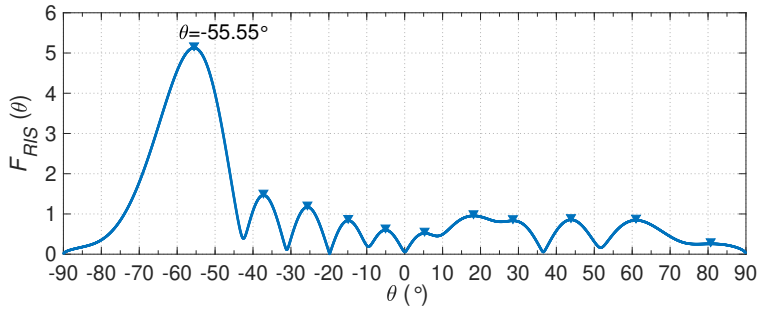

(b) The measured beamspace domain of the incident wireless signal on RIS 2 when the user is located at $(0\,\mathrm{m}, 1.0\,\mathrm{m})$

Fig. 11. The measurement results of the proposed AoA estimation method for RIS.

During the experimental measurement, the antenna of the user, the two RIS panels, and the two receiving antennas of the access point are all positioned at the same horizontal height.

The experiment was conducted in an indoor environment. To evaluate the system's positioning performance, a two-dimensional coordinate system was established, with the centers of RIS 1 and RIS 2 located at the coordinate points $(1.5\,\mathrm{m}, 0\,\mathrm{m})$ and $(-1.5\,\mathrm{m}, 0\,\mathrm{m})$, respectively. As illustrated in Fig. 10, a total of 72 test points were selected in the two-dimensional coordinate system, with each blue dot representing a test point. During the measurement at each test point, the user's antenna was placed at the corresponding coordinate for the measurement validation.

1) Validation of Estimation Method of RIS AoA: We conducted experimental measurement to validate the proposed AoA estimation method for RIS. The user's antenna was first placed at coordinates $(-0.5\,\mathrm{m}, 3.5\,\mathrm{m})$. According to the geometric relationship of the coordinates, the exact value of the AoA of RIS 1 is $29.74°$. The prototype system performed real-time processing of the 16 odd-order harmonic components of the signals received by antenna 1, estimating the channel vector from the user to RIS 1. Based on equation (27), the beamspace domain of the

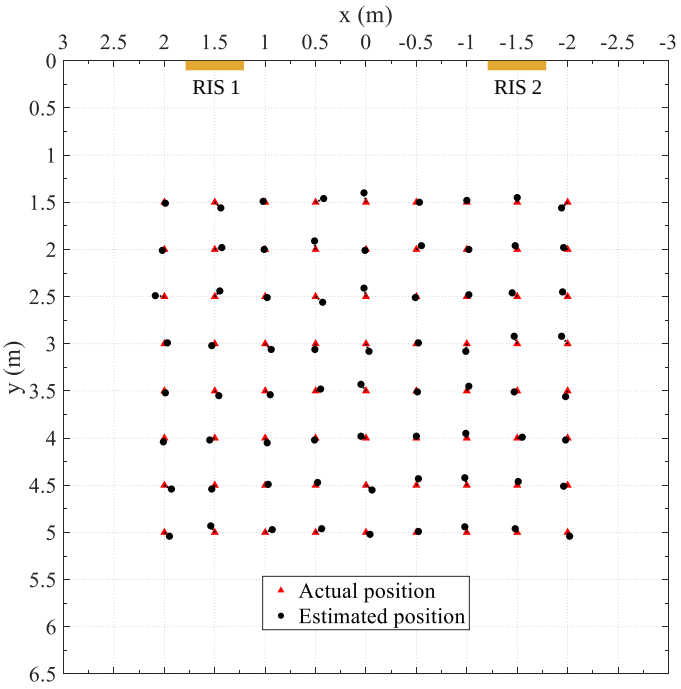

Fig. 12. The measurement results of user positioning of the prototype system.

incident wireless signal on RIS 1 was further obtained, as shown in Fig. 11(a). It can be observed that in this measurement case, the estimated AoA was $\widetilde{\theta} = 30.20°$. and the prototype system has an AoA estimation error of less than $1°$ (i.e., $30.20 - 29.74 = 0.46°$).

Then the user's antenna was placed at coordinates $(0\,\mathrm{m}, 1.0\,\mathrm{m})$. According to the geometric relationship of the coordinates, the exact value of the AoA of RIS 2 is $-56.31°$. The prototype system performed real-time processing of the 16 odd-order harmonic components of the signals received by antenna 2, obtaining the beamspace domain of the incident wireless signal on RIS 2 as shown in Fig. 11(b). It can be observed that in this measurement case, the estimated AoA was $\widetilde{\theta} = -55.55°$. and the prototype system has an AoA estimation error of less than $1°$ (i.e., $56.31 - 55.55 = 0.76°$). The above experimental results validate the feasibility of the proposed RIS-based wireless sensing functionality to accurately estimate the AOA of incident signals.

2) Validation of RIS-based Positioning Scheme: To comprehensively evaluate the positioning performance of the prototype system, the user was placed at the 72 test points shown in Fig. 10. The aforementioned measurements were conducted for each test point, with the estimated positioning values recorded according to equations (15) and (16). The experimental results are shown in Fig. 12, where the red triangle dots represent the actual positions of the user during

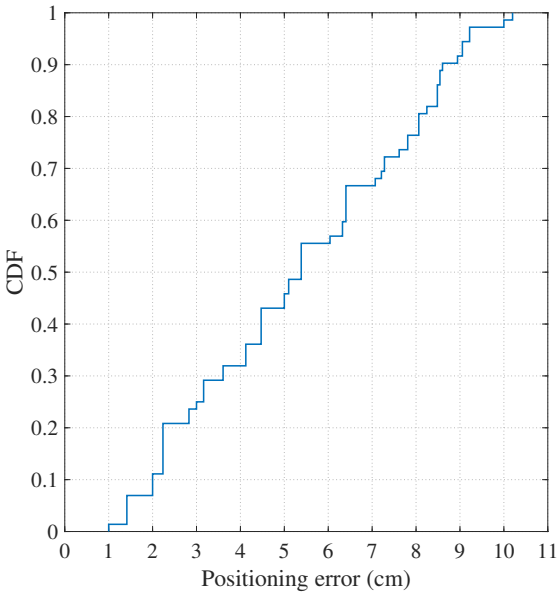

Fig. 13. The measured CDF of user positioning errors of the prototype system.

the 72 measurements, distributed within an area of $4 \times 3.5\,\mathrm{m}^2$. The corresponding black dots represent the positions of the user estimated by the RIS-based sensing and positioning prototype system, demonstrating the effective realization of user positioning functionality.

As shown in Fig. 13, to quantify the measured performance of the RIS-based sensing and positioning prototype system, the experimental results at 72 test points are statistically analyzed and the cumulative distribution function (CDF) curve of user positioning errors is obtained. The measured CDF curve indicates that all the positioning errors are less than $10.2\,\mathrm{cm}$, with 43.06% of the test points having positioning errors under $5\,\mathrm{cm}$ and 97.22% under $10\,\mathrm{cm}$, suggesting that the prototype system achieves centimeter-level positioning accuracy. The measurement results validate the feasibility of the proposed RIS-based wireless signal sensing method and positioning scheme, showing the potential to expand the application scenarios of RIS-assisted wireless communication systems

VI. Conclusion

In this paper, we have introduced an RIS-based wireless signal sensing method under the constraint of passive reflection characteristics of RIS. By performing space-time coding matrix on the RIS, its spatial dimension information is transformed into the frequency domain. This

enables efficient estimation of the AoA of the incident signals on the RIS, and it only requires a single-channel received signal at the access point. The proposed method has been proven to be robust against the non-ideal angle-sensitive reflection coefficients of the RIS. On this basis, a sensing and positioning prototype system based on two millimeter-wave RIS panels has been designed and implemented. The measurement results demonstrate that the prototype system achieves centimeter-level positioning accuracy with an error of less than $10\,\mathrm{cm}$ in 97.22% of the cases. The proposed method and scheme hold the potential to expand the application scenarios of RIS and promote the integration of future communication and sensing technologies.

APPENDIX A - PROOF OF THEOREM 1

If the time-domain sequence given in equation (7) forms a periodic sequence, then its exponential Fourier series expansion is expressed as

$$\Gamma_{n,m}(t) = \sum_{l=-\infty}^{\infty} b_{n,m}^{l} e^{j\frac{2\pi}{T_s}lt}, \tag{35}$$

where

$$\begin{aligned}
b_{n,m}^{l} &= \frac{1}{T_s}\int_0^{T_s} \Gamma_{n,m}(t)\, e^{-j\frac{2\pi}{T_s}lt} dt \\
&= \frac{1}{T_s}\int_0^{T_s} \sum_{q=1}^{Q} \Gamma_{n,m}^{q} R\left(t-(q-1)\frac{T_s}{Q}\right) e^{-j\frac{2\pi}{T_s}lt} dt \\
&= \frac{1}{T_s}\sum_{q=1}^{Q}\int_{\frac{(q-1)T_s}{Q}}^{\frac{qT_s}{Q}} \Gamma_{n,m}^{q} e^{-j\frac{2\pi}{T_s}lt} dt \\
&= \frac{1}{T_s}\sum_{q=1}^{Q}\frac{jT_s\Gamma_{n,m}^{q}}{2\pi l}\left(e^{-j2\pi l\frac{q}{Q}} - e^{-j2\pi l\frac{q-1}{Q}}\right) \\
&= \frac{1}{T_s}\sum_{q=1}^{Q}\frac{jT_s\Gamma_{n,m}^{q}}{2\pi l} e^{-j\pi l\frac{2q-1}{Q}}\left(e^{-j\frac{\pi l}{Q}} - e^{j\frac{\pi l}{Q}}\right) \\
&= \sum_{q=1}^{Q}\frac{\Gamma_{n,m}^{q}}{\pi l} e^{-j\pi l\frac{2q-1}{Q}}\sin(\frac{\pi l}{Q}) \\
&= \frac{1}{Q}\mathrm{sinc}(\frac{\pi l}{Q})\sum_{q=1}^{Q}\Gamma_{n,m}^{q} e^{-j\pi\frac{2q-1}{Q}l}.
\end{aligned} \tag{36}$$

By substituting equations (35) and (36) into equation (6), we obtain

$$\begin{aligned} y(t) &= \left(\sum_{m=1}^{M} \sum_{n=1}^{N} h_{n,m} \Gamma_{n,m}(t) g_{n,m} + h_D \right) \sqrt{p} + w \\ &= \left(\sum_{m=1}^{M} \sum_{n=1}^{N} h_{n,m} \sum_{l=-\infty}^{\infty} b_{n,m}^{l} e^{j\frac{2\pi}{T_s} lt} g_{n,m} + h_D \right) \sqrt{p} + w \\ &= \sum_{l=-\infty}^{\infty} \left(\sum_{m=1}^{M} \sum_{n=1}^{N} h_{n,m} b_{n,m}^{l} g_{n,m} e^{j\frac{2\pi}{T_s} lt} \right) \sqrt{p} + h_D \sqrt{p} + w, \end{aligned} \tag{37}$$

According to equation (37), the signal component of the l-th order harmonic received by the access point is

$$Y'_l = \sum_{m=1}^{M} \sum_{n=1}^{N} h_{n,m} b_{n,m}^{l} g_{n,m} \sqrt{p}, \tag{38}$$

The sequence given in equation (7) is a non-periodic sequence. The above analysis is a Fourier expansion after it has been periodically extended. Therefore, within this non-periodic sequence duration, the l-th order harmonic component of the received signal of the access point is

$$Y_l = \sum_{m=1}^{M} \sum_{n=1}^{N} h_{n,m} a_{n,m}^{l} g_{n,m} \sqrt{p} + W_l, \tag{39}$$

where $a_{n,m}^{l} = T_s b_{n,m}^{l}$. Theorem 1 is obtained by arranging equation (39) into matrix form.

REFERENCES

[1] F. Tariq, M. R. A. Khandaker, K.-K. Wong, M. Imran, M. Bennis, and M. Debbah, "A speculative study on 6G," *IEEE Wireless Commun.*, vol. 27, no. 4, pp. 118-125, Aug. 2020.

[2] M. Di Renzo *et al.*, "Smart radio environments empowered by reconfigurable intelligent surfaces: How it works, state of research, and the road ahead," *IEEE J. Sel. Areas Commun.*, vol. 38, no. 11, pp. 2450-2525, Nov. 2020.

[3] J. Yang, C. K. Wen, X. Yang, J. Xu, T. Du, and S. Jin, "Multi-domain cooperative SLAM: The enabler for integrated sensing and communications," *IEEE Wireless Commun.*, vol. 30, no. 1, pp. 40-49, Feb. 2023.

[4] Q. Wu, S. Zhang, B. Zheng, C. You, and R. Zhang, "Intelligent reflecting surface-aided wireless communications: A tutorial," IEEE Trans. Commun., vol. 69, no. 5, pp. 3313-3351, May 2021.

[5] H. Wymeersch, J. He, B. Denis, A. Clemente, and M. Juntti, "Radio localization and mapping with reconfigurable intelligent surfaces: Challenges, opportunities, and research directions," *IEEE Veh. Technol. Mag.*, vol. 15, no. 4, pp. 52-61, Dec. 2020.

[6] H. Zhang, B. Di, K. Bian, Z. Han, H. V. Poor, and L. Song, "Toward ubiquitous sensing and localization with reconfigurable intelligent surfaces," *Proc. of the IEEE*, vol. 110, no. 9, pp. 1401-1422, Sept. 2022.

[7] J. He, H. Wymeersch, L. Kong, O. Silvén, and M. Juntti, "Large intelligent surface for positioning in millimeter wave MIMO systems," *2020 IEEE 91st Veh. Technol. Conf, 2020*, May. 2020, pp. 1-5.

[8] H. Wymeersch and B. Denis, "Beyond 5G wireless localization with reconfigurable intelligent surfaces," *2020 IEEE Int. Conf. on Commun.*, Jun. 2020, pp. 1-6.

[9] J. Zhang, Z Zheng, Z Fei, and X Bao, "Positioning with dual reconfigurable intelligent surfaces in millimeter-wave MIMO systems," *IEEE/CIC International Conference on Communications in China*, Aug. 2020, pp. 1-6.

[10] W. Wang and W. Zhang, "Joint beam training and positioning for intelligent reflecting surfaces assisted millimeter wave communications," *IEEE Trans. Wireless Commun.*, vol. 20, no. 10, pp. 6282-6297, Oct. 2021.

[11] H. Zhang, H. Zhang, B. Di, K. Bian, Z. Han, and L. Song, "Metalocalization: Reconfigurable intelligent surface aided multi-user wireless indoor localization," *IEEE Trans. Wireless Commun.*, vol. 20, no. 12, pp. 7743-7757, Dec. 2021.

[12] A. Elzanaty, A. Guerra, F. Guidi, and M. -S. Alouini, "Reconfigurable intelligent surfaces for localization: Position and orientation error bounds," *IEEE Trans. Signal Process.*, vol. 69, pp. 5386-5402, 2021.

[13] Z. Chen, J. Tang, L. Huang, Z. Q. He, K. K. Wong, and J. Wang, "Robust target positioning for reconfigurable intelligent surface assisted MIMO radar systems," *IEEE Trans. Veh. Technol.*, vol. 72, no. 11, pp. 15098-15102, Nov. 2023.

[14] T. Ma, Y. Xiao, X. Lei, W. Xiong, and M. Xiao, "Distributed reconfigurable intelligent surfaces assisted indoor positioning," *IEEE Trans. Wireless Commun.*, vol. 22, no. 1, pp. 47-58, Jan. 2023.

[15] H. Zhang, J. Hu, H. Zhang, B. Di, K. Bian, Z. Han, and L. Song, "MetaRadar: Indoor localization by reconfigurable metamaterials," *IEEE Trans. Mobile Comput.*, vol. 21, no. 8, pp. 2895-2908, Aug. 2022.

[16] W. Y. Chung, L. H. Shen, K. T. Feng *et al.*, "WiRiS: Transformer for RIS-assisted device-free sensing for joint people counting and localization using Wi-Fi CSI," *2023 IEEE 34th Annu. Int. Symp. on PIMRC*, 2023, pp. 1-6.

[17] L. Bai, H. Cao, T. Bai, and C. He, "1-bit programmable metasurface-based 2-D direction finding," *IEEE Antennas and Wireless Propag. Lett.*, vol. 22, no. 9, pp. 2160-2164, Sep. 2023.

[18] Z. Chen, P. Chen, L. Zheng, and Y. Zhang, "DNN-DANM: A high-accuracy two-dimensional DOA estimation method using practical RIS," *IEEE Trans. Veh. Technol.*, vol. 73, no. 2, pp. 1792-1802, Feb. 2024.

[19] M. Rahal, B. Denis, T. Mazloum, F. Munoz, and R. D'Errico, "RIS-aided positioning experiments based on mmWave indoor channel measurements," *2023 13th Int. Conf. IPIN*, 2023, pp. 1-6.

[20] G. Zhang, D. Zhang, H. Deng, Y. Wu, F. Zhan, and Y. Chen, "Practical passive indoor localization with intelligent reflecting surface," *IEEE Trans. Mobile Comput.*, vol. 23, no. 12, pp. 12477-12490, Dec. 2024.

[21] L. Zhang, X. Q. Chen, S. Liu *et al.*, "Space-time-coding digital metasurfaces," *Nature Communications*, vol. 9, no. 1, pp. 1–11, Oct. 2018.

[22] J. Y. Dai, L. X. Yang, J. C. Ke *et al.*, "High-efficiency synthesizer for spatial waves based on space-time-coding digital metasurface," *Laser & Photonics Reviews*, vol. 14, no. 6, Art. no. 1900133, 2020.

[23] L. Zhang, M. Z. Chen, W. Tang *et al.*, "A wireless communication scheme based on space- and frequency-division multiplexing using digital metasurfaces," *Nature Electronics*, vol. 4, no. 3, pp. 218–227, Mar. 2021.

[24] W. Tang, J. Y. Dai, M. Z. Chen *et al.*, "MIMO transmission through reconfigurable intelligent surface: System design, analysis, and implementation," *IEEE J. Sel. Areas Commun.*, vol. 38, no. 11, pp. 2683–2699, Nov. 2020.

[25] J. Wang, W. Tang, J. C. Liang *et al.*, "Reconfigurable intelligent surface: Power consumption modeling and practical measurement validation," *IEEE Trans. Commun.*, vol. 72, no. 9. pp. 5720–5734, Sept. 2024.

[26] W. Tang, X. Chen, M. Z. Chen, J. Y. Dai, Y. Han, S. Jin, Q. Cheng, G. Y. Li, and T. J. Cui, "On channel reciprocity in reconfigurable intelligent surface assisted wireless networks," *IEEE Wireless Commun.*, vol. 28, no. 6, pp. 94–101, 2021.

[27] W. Tang, X. Chen, M. Z. Chen *et al.*, "Path loss modeling and measurements for reconfigurable intelligent surfaces in the millimeter-wave frequency band," *IEEE Trans. Commun.*, vol. 70, no. 9, pp. 6259-6276, Sep. 2022.

[28] W. Chen, L. Bai, W. Tang, S. Jin, W. X. Jiang, and T. J. Cui, "Angle-dependent phase shifter model for reconfigurable intelligent surfaces: Does the angle-reciprocity hold?" *IEEE Commun. Lett.*, vol. 24, no. 9, pp. 2060-2064, Sep. 2020.

[29] W. Tang *et al.*, "Wireless communications with reconfigurable intelligent surface: Path loss modeling and experimental measurement," *IEEE Trans. Wireless Commun.*, vol. 20, no. 1, pp. 421-439, Jan. 2021.

[30] S. Yue, S. Zeng, H. Zhang, F. Lin, L. Liu, and B. Di, "Intelligent omni-surfaces aided wireless communications: Does the reciprocity hold?" *IEEE Trans. Veh. Technol.*, vol. 72, no. 6, pp. 8181-8185, Jun. 2023.